P and S wave travel time tomography of the SE Asia-Australia collision zone

Aristides Zenonos[a], Luca De Siena[a], Nicholas Rawlinson[b]

[a]*School of Geosciences, University of Aberdeen, Aberdeen, AB24 3UE, UK*
[b]*Department of Earth Sciences, University of Cambridge, Cambridge, CB2 3EQ, UK*

Abstract

The South-East (SE) Asia - Australia collision zone is one of the most tectonically active and seismogenic regions in the world. Here, we present new 3-D P- and S-wave velocity models of the crust and upper mantle by applying regional earthquake travel-time tomography to global catalogue data. We first re-locate earthquakes provided by the standard ISC-Reviewed and ISC-EHB catalogues using a non-linear oct-tree scheme. A machine learning algorithm that clusters earthquakes depending on their spatiotemporal density was then applied to significantly improve the consistency of ~~travel time~~ travel-time picks. We used the Fast Marching Tomography software package to retrieve ~~3D~~ 3-D velocity and interface structures from starting 1-D velocity and Moho models. Synthetic resolution and sensitivity tests demonstrate that the final models are robust, with P-wave speed variations (∼130 km horizontal resolution) generally recovered more robustly than S-wave speed variations (∼220 km horizontal resolution). The retrieved crust and mantle anomalies offer a new perspective on the broad-scale tectonic setting and underlying mantle architecture of SE Asia. While we observe clear evidence of subducted slabs as high velocity anomalies penetrating into the mantle along the Sunda arc, Banda arc and Halmahera arc, we also see evidence for slab gaps or holes in the vicinity of east Java. Furthermore, a high-velocity region in the mantle lithosphere connects northern Australia with Timor and West Papua. The S-wave model shows broad-scale features similar to those of the P-wave model, with mantle earthquakes generally distributed within high-velocity slabs. The high velocity mantle connection between northern Australia and the eastern margin of the Sunda Arc is also present in the S-wave model. While the S-wave model has a lower resolution than the P-wave model due to the availability of fewer paths, it nonetheless provides new and complementary insights into the structure of the upper mantle

beneath southeast Asia.

Keywords: tomography, travel-time, body-wave, SE Asia, earthquakes

1. Introduction

The southern region of the Eurasian plate comprises the continental core of southeast Asia, and is bounded by the Indo-Australian, Pacific and Philippines plates (Figure 1). Significant relative plate motions in the region have created a complex and dynamic setting that encompasses processes such as orogenesis, subduction, crustal accretion, rapid exhumation, megathrust earthquakes and volcanism (Figures 1, 2). Subduction has been the dominant plate-tectonic process in the region since the Mesozoic (Hall, 1997, 2012), with thousands of kilometres of lithosphere subducted into the mantle (e.g. the Tethyan Ocean) while the Australian and Pacific plates moved in northward and westward directions, respectively (Hall and Spakman, 2015). These complex subduction processes are the cause of intense seismicity, which can be used to image the seismic structure of the region in detail.

[Figure 1 Boundaries]

Seismic tomography has been widely used to better understand the lithospheric structure and tectonic evolution of southeast Asia and the surrounding region (Hamilton, 1974, 1979; Fukao et al., 1992; Puspito et al., 1993; Widiyantoro and van der Hilst, 1997; Hafkenscheid et al., 2001; Lebedev and Nolet, 2003; Replumaz et al., 2004; Amaru, 2007; Pesicek et al., 2008, 2010; Hall and Spakman, 2015). While these models are broadly similar, they can lose consistency in regions of small-scale heterogeneity such as subduction zones. The most recent regional interpretation for SE Asia was given by Hall and Spakman (2015). They used the global P-wave model UU-P07 from Amaru (2007) where the most prominent subduction zone was imaged along the Sunda-Banda arc (Sumatra, Java and Banda islands). They suggested that the simplest subduction segment spans the region between West to East Java (Figure 1) and has a relative convergence of 7cm/year and a gap between the trench and volcanic-arc of about 300 km. The initial angle of the slab is estimated

Email address: a.zenonos@abdn.ac.uk (Aristides Zenonos)

to be around 20° along the trench-volcanic arc before the slab dips more steeply, at around 60°-70° at a depth of about 150 km.

In contrast, subduction beneath the region east of Java appears to be more complicated due to the presence of a seismicity gap between 250 and 500 km depth, the origin of which is debated. Widiyantoro et al. (2011) propose that the gap is a hole in the subducted slab with an along-strike length of about 400 km. Hall and Spakman (2015) note that the aseismic region of the slab is structural, e.g., thinning of lithospheric mantle, either created during or prior to the subduction. Alternatively, the seismic gap in the subducting slab might have originated from a strong compositional heterogeneity which reduced the rigidity of the lithosphere, making ~~the~~ earthquakes less likely (Hall and Spakman, 2015); however, there is little evidence to support this hypothesis. Widiyantoro et al. (2011) also interpret a second (but smaller) hole located east of the first gap (between about 200 and 400 km depths, with an along-strike length of about 150 km) as a feature caused by slab necking. Hall (2009) proposed that these holes resulted from a buoyant thickened oceanic crust, like the Roo Rise (Kopp et al., 2006), which arrived at the subduction trench at East Java from the south. This buoyant object entered the trench producing a slab tear and subducted together with the rest of the lithosphere, thus producing a hole in the slab highlighted by Widiyantoro et al. (2011). However, Hall and Spakman (2015) describe an alternative procedure for the creation of the tear based on a buoyant object locally blocking the subduction process resulting in a disconnected slab subducting on either side of it. It has been speculated that this object was the Roo Rise (Simandjuntak and Barber, 1996); however, Hall and Spakman (2015) disagree due to the dimension and position of the hole which implies that it was created about 8 Ma ago.

The northwest segment of the Sunda arc near Sumatra is parallel to the relative motion between India and SE Asia. The subduction beneath Sumatra is partitioned into two segments with a possible slab tear or fold between them. Hall and Spakman (2015) interpret the low-velocity anomalies in the middle of Sumatra as a slab tear, while Pesicek et al. (2008, 2010) interpret the slab in this region to have the form of a NNE- to NE-plunging fold. The tear or fold divides the trench-normal subduction and the trench-parallel movement in Sumatra. The Pesicek et al. (2008) and Hall and Spakman (2015) tomographic models are similar in this region, but the interpretation has one notable difference in the Benioff zone contours. Pesicek et al. (2008) proposed that the

Benioff zone extends from Sumatra beneath the Malay peninsula while Hall and Spakman (2015) limits its extension to the Malaysian coast. Essentialy, the interpretation of Pesicek et al. (2008) states that the Benioff zone contours extend further NE compared to the interpretation of Hall and Spakman (2015). Hall and Spakman (2015) observed that the slab dips more strongly north of the tear or fold compared to the south. The NNE-trending tear or fold thus separates subduction in the west which penetrates into the lower mantle (down to 800 km) from subduction in the east, which penetrates into the transition zone (down to 550 km).

Seismicity in the region of the Banda Arc exhibits a strongly curved Benioff zone. Two major contrasting explanations are often given for the shape of the Benioff zone; one suggests a single curved subducting slab (Spakman and Hall, 2010; Hall and Spakman, 2015) while the other suggests the presence of double subduction from north and south (Cardwell and Isacks, 1978; Das, 2004). Based on tomographic images (Hall and Spakman, 2015) it is observed that the slab is totally confined to the upper mantle. Widiyantoro and van der Hilst (1997) describe the slab geometry as spoon-shaped. The slab has the form of a lithospheric fold which bends west and has a flat-lying portion which sits at the bottom of the upper-mantle. Some authors support the two-slab model (Cardwell and Isacks, 1978; Das, 2004) basing their interpretation on the complex spatial variation of the focal mechanisms. Hamilton (1979); Charlton (2000); Milsom (2001); Spakman and Hall (2010); Hall and Spakman (2015) suggest that the subduction is due to a bent and deformed single slab. Hall and Spakman (2015) propose that the Banda slab is caused by rollback into the Banda embayment which is part of the Australian continent rather an extension of a single long-lived subduction zone north of Australia. The strong seismic activity in the region's upper mantle indicates a folded surface. For Spakman and Hall (2010), the rollback of the Banda embayment is based on the measured age of the backarc basins, which show evidence of a young subduction history entirely confined to the upper mantle. The areas surrounding the Banda Sea (Sunda, Sulawesi) feature subduction which penetrates into the lower mantle, which points to a different evolution mechanism. As the Australian plate moved northward at high speed (7 cm/yr), the increasing resistance of the mantle to plate motion may have progressively folded the slab, causing this curved subduction zone (Spakman and Hall, 2010).

The Molucca Sea is of particular interest because it is the only active arc - arc collision in southeast Asia. The inverted U-shape formed by the two subducting slabs has been recognised for many years (e.g. Puspito et al. (1993)). The collision comprises two subducting slabs dipping east (Halmahera) and west (Sangihe) below the two respective volcanic arcs. Both earthquake location and tomographic studies indicate that the west-dipping slab reaches the bottom of the upper-mantle (down to about 650 km) and has an overall dip angle of 45° (Hatherton and Dickinson, 1969; Puspito et al., 1993). On the other hand, the Halmahera slab only appears to penetrate to a depth of 400 km (Hall and Spakman, 2015).

In the P-wave ~~travel time~~ travel-time tomography study of the region by Hall and Spakman (2015) the authors invoke thermal processes at subduction zones to explain many of the velocity anomalies present in their model. It is well known that the recovery of both P- and S-velocities better constrains the thermal state of the lithosphere compared to P-velocity alone (Goes et al., 2000). While high temperatures lower both types of velocities, P- and S-waves have different sensitivities to temperature and composition (Trampert et al., 2001). Therefore, having both types of velocity available improves the likelihood of untangling their relative contributions, which in turn may provide more insight into subduction and other plate tectonic processes.

In this paper, we construct high-resolution (∼130 km ∼220 km for P- and S-wave respectively) 3-D seismic models of the crust and upper mantle beneath the SE Asia - Australia collision zone by inverting both P- and S-wave arrival times. The models use all available arrival times from earthquake-station pairs in the region of interest that have been archived in ~~international seismic data repositories~~ the International Seismological Centre (ISC) over the last 35 years. A data-processing strategy based on unsupervised machine learning (Ester et al., 1996; Pedregosa et al., 2012) selects and weights the arrival times used in the inversion for seismic velocities. We applied a non-linear location method (NLL) (Lomax et al., 2009) to obtain reliable source locations for subsequent use in the Fast Marching Method (FMM) (Sethian and Popovici, 1999; Rawlinson and Sambridge, 2004a; de Kool et al., 2006), which is used to solve the forward problem. An iterative non-linear inversion scheme is applied to constrain velocities and interfaces in the crust and mantle beneath SE-Asia. The models obtained with NLL are tested against those obtained using the ISC-Reviewed and ISC-EHB datasets. We also test the influence of using the 3-D crust1.0 (Laske et al., 2013) velocity model for the crust as a starting model, compared to the 1-D reference model ak135

(Kennett et al., 1995). Finally, we examine our results in light of previous seismic wavespeed models of the region.

2. Data

Frequent high-magnitude earthquakes in the study area underpin the high-quality body-wave arrival-time data available from the catalogues. The arrival times and source locations were downloaded from the International Seismological Centre (ISC). The ISC Bulletin is an ideal source of global arrival times as it comprises the largest collection of freely available seismic data. In this study, we have used both the ISC-Reviewed (Engdahl and Gunst, 1966) dataset and the updated ISC-EHB dataset, which is a groomed version of the ISC Bulletin, containing seismic events from 1960 to 2013. The review procedure for the ISC-Reviewed dataset checks that the hypocentre is in the seismic region for the reported arrivals and reports missing data, magnitude, phase-time residuals and outliers. The improved dataset produced by Engdahl et al. (1998) and Weston et al. (2018) benefits from phase re-identification of ISC arrivals and source relocation based on the 1-D ak135 velocity model (Kennett et al., 1995). By using NLL (Lomax and Curtis, 2001; Lomax et al., 2001, 2009) on both datasets we obtained two more datasets, making four in total, which from now on will be referred to as NLL-ISC-Reviewed and NLL-ISC-EHB since they are based on the ISC-Reviewed and ISC-EHB datasets respectively. However, these datasets are not entirely independent, since they share many of the same picked arrival times.

We used the selection criteria devised by Amaru (2007) to refine our dataset. For P-wave arrivals we set maximum residuals of ±7.5 s and ±3.5 s for epicentral distances of less and more than 25°, respectively. For S-wave arrivals we set our maximum residual to ±7.5 s irrespective of epicentral distance. The selection criteria are sourced from Bijwaard et al. (1998) in which they compute the density of travel-time residuals versus the epicentral distance and state that they no longer display the well-known dependence of ISC delay times on epicentral distance that indicates deviations of the reference model velocities from the layered averaged real Earth. The precision of the P phases was estimated following the method of Gudmundsson et al. (1990). The aforementioned criteria eliminate approximately 7.2%, which amounts to 444514 arrivals from an original pool of 478822. The resultant number of picks obtained using these thresholds are summarised in Table 1.

[Figure 2 Earthquakes]

[Figure 3 Stations]

Overall, 12 (eight P-wave and four S-wave) tomographic models were produced and compared to investigate the robustness of our results. The differences between the various models are summarised in Table 1. Crustal phases Pb/Sg and Pg/Sg were incorporated in models P_F and S_C to determine whether the constraints they provide on crustal structure have any influence on the recovery of the mantle structure. In particular, we test whether our mantle model features any significant change if we jointly invert for crust and mantle velocity structure or simply invert for mantle velocities alone. The starting models crust1.0 and ak135 were produced by Laske et al. (2013) and Kennett et al. (1995), respectively.

[Table 1 Models]

As seen in Table 1, the number of picks for NLL datasets are more than the ISC-Reviewed-R and ISC-EHB-R datasets for the P_A and P_B models. This is because the reduced ISC-Reviewed-R and ISC-EHB-R catalogues are a subset of the initial ISC-Reviewed and ISC-EHB datasets respectively which only include picks contained in the final NLL solution, subject to the selection criteria described previously (threshold on residual). For P_E, P_F, P_G and S-wave models we only use the ISC-EHB dataset since in these cases we would like to include as many data as possible. The number of events and receivers ranges from 16490-30360 and 511-665 respectively and the specific number of picks per model can be found in Table 1.

3. Method

3.1. Non-linear earthquake location

A Non-Linear Location method with Oct-Tree importance sampling (Lomax and Curtis, 2001; Lomax et al., 2001) was used for earthquake location prior to tomographic inversion. The Oct-Tree algorithm provides the maximum likelihood location from the non-linear posterior Probability Density Function (PDF) of the events. The PDF can also be used to define the spatial uncertainty on the location (see Figure S1). The ISC-Reviewed and ISC-EHB datasets were relocated using NLL. For the final event locations we used the "Global Mode" of NLL (Lomax et al., 2009), which is in spherical coordinates and uses a minimum of 40 arrivals for each event. The maximum hypocentre Root-Mean-Square (RMS) is set to 10s, which restricts the accepted relocated events to those which have their phase arrival RMS below 10 seconds. These criteria resulted in a reduction to 41250 from 49206 events for the ISC-EHB catalogue and to 61358 from 322922 events for the ISC-Reviewed catalogue. This is expected since the ISC-EHB catalogue is a groomed version of the data ~~rather than~~ compared to the ISC-Reviewed catalogue, which includes lower quality data from 1900 onward with, in some cases, only a few inaccurate arrivals associated with each event. Compared to the ISC catalogues, our use of NLL to determine hypocenters and origin times is completely automated i.e. there is no manual intervention by an analyst. As such, we found that a minimum threshold of at least 40 arrivals per event was necessary to ensure stable relocations. Below that number, we found that the location uncertainty of some events was very high. By generating an ensemble of tomographic models using a number different but arguably robust datasets (defined by different source locations, different numbers of arrivals, but overlapping arrival time picks), we have a means of assessing the robustness of features that we choose to interpret.

3.2. Improving Signal to Noise ratio (S/N) using unsupervised machine learning

In order to improve the S/N ratio and reduce redundancy in the data and compute time required for the inversion we automatically determine ray bundles which are then used to form summary rays. To do so, we modified the approach of Bijwaard et al. (1998) using unsupervised machine learning. In their study, Bijwaard et al. (1998) formed ray bundles for similar raypaths and applied a weighting factor to each bundle using the formula

$$W_{rb}^{-1} = \sqrt{\frac{\sum_{i=1}^{N}(\overline{dt} - dt_i)^2}{N}} \quad (1)$$

where W_{rb} represents the ray bundle weight, dt_i is the delay of ray i, $\overline{dt}$ is the average delay time of the ray bundle and N is the total number of rays in the bundle. Hence, similar raypaths are de-clustered by grouping them together, leaving only one raypath for a specified source-receiver pair. The final raypath is assigned a weighting factor, W_{rb} based on the ~~travel time~~ travel-time residuals of the raypaths within the cluster. The weighting factors were restricted to vary by less than one order of magnitude. We ~~also~~ modified the cell division for the ray bundles ~~, following~~ of Amaru (2007), who used a $0.3° \times 0.3° \times dz$ cell size for the ray bundles with dz increasing from 15 km at the surface to 40 km at 660 km depth. ~~Unsupervised~~ To determine the ray bundles or clusters, unsupervised machine learning was implemented using the scikit-learn tool (Pedregosa et al., 2012) and the Density-Based SCANning (DBSCAN) algorithm of Ester et al. (1996). After transforming geographic into Cartesian coordinates, we initially set (1) maximum permitted distance between the clusters to 0.3° and (2) minimum number of events in each cluster to two. The Cartesian coordinates and the ~~travel times~~travel-times, which are known as "features" in machine learning (Ester et al., 1996) are then used for clustering events. These features are calibrated to cluster events whose location and ~~travel time~~ travel-time should be consistent with each other. In other words, events which are found in a similar location in space with similar arrival times at the same receiver are grouped together. The new clusters include sources that are detected as "close sources" for the same receiver. We therefore follow a de-clustering approach (Pyrcz and Deutsch, 2002) where the identified "close sources" form the ray bundle associated with a weighting uncertainty.

~~This~~ The purpose of unsupervised machine learning is to detect hidden patterns in the dataset without the need for any training algorithm. The new DBSCAN machine learning approach enhances the quality of the generated ray bundles. It takes into consideration a number of attributes of the data, in particular the euclidean distances across all four dimensions ~~of all the data points~~ (x,y,z location and the ~~travel time). This is an objective and quantitative measure of how close the points are to each other, with DBSCAN clustering together points that are close together in space. Since we are initially unsure about the number of ray bundles which exist in our dataset, DBSCAN can identify this number using a density-based approach rather than grouping events within a fixed distance to each other~~travel-time). Here, we include the spatiotemporal location of the events which we are unsure about their (location and travel-time) exact relationship. DBSCAN identifies the outliers in a dataset, which in our case are the raypaths which do not form a ray bundle. If a group of events are found in a similar position and one has an anomalous travel-time, then this particular event gets the highest uncertainty and the others gets the uncertainty based on the formula 1. More importantly, raypaths which carry similar information, i.e., found to have a similar source-station pair and ~~travel time~~travel-time, do not contribute explicitly to our model, but do reduce the data noise (assuming that it is random) and time required for inversion (see Figure ~~S1~~ S2 for a demonstration of the effectiveness of this approach). By doing so, we don't have to employ low-quality single rays in our model and thus, the ray bundles are of higher quality. The DBSCAN algorithm is used in a variety of scientific areas from participatory sensing (Zenonos et al., 2018) to astronomy (Daruru et al., 2010) to obtain hidden patterns in the dataset. DBSCAN does not previously require to pre-set the number of existing clusters in our dataset. It can identify this number using a density-based approach rather than grouping events within a fixed distance, as done by Bijwaard et al. (1998). On the other hand, DBSCAN requires the minimum number of raypaths needed to form a ray bundle (cluster) and the maximum permitted distance between the raypaths to form a cluster. We present the DBSCAN approach as a method alternative to Bijwaard et al. (1998) for grouping similar raypaths together and it is not necessarily a better method.

3.3. Iterative non-linear tomographic inversion

We performed an iterative non-linear tomographic inversion for Vp and Vs variations by applying the software package FMTOMO (Rawlinson and Sambridge, 2004a,b). FMTOMO uses the Fast Marching Method (Sethian, 1996; Sethian and Popovici, 1999) for the forward step of ~~travel time~~ travel-time prediction in which the eikonal equation is solved on a grid of points. The main advantages of this method are robustness in the presence of extreme heterogeneity and computational efficiency, particularly when the ratio of sources to receivers is $>> 1$ or $<< 1$ (Rawlinson et al., 2008). Due to the large size of our southeast Asian dataset, the forward step was executed in parallel mode on a cluster computer in order to reduce the computing time. FMTOMO uses a subspace inversion scheme (a gradient-based technique) (Kennett et al., 1988) to solve the linearised inversion step which includes damping and smoothing regularisation. The ~~iterative~~ sequential application of the forward and inversion steps iteratively solves the non-linear problem ~~.~~ since ray path geometries are updated after each application of the subspace inversion scheme. The objective function that is minimised has the form:

$$S(\mathbf{m}) = (g(\mathbf{m}) - \mathbf{d}_{obs})^T \mathbf{C}_d^{-1} (g(\mathbf{m}) - \mathbf{d}_{obs}) + \epsilon(\mathbf{m} - \mathbf{m}_0)^T \mathbf{C}_m^{-1} (\mathbf{m} - \mathbf{m}_0) + \eta \mathbf{m}^T \mathbf{D}^T \mathbf{D} \mathbf{m} \quad (2)$$

where, $\mathbf{g(m)}$ are the predicted residuals, $\mathbf{d}_{obs}$ are the observed residuals, $\mathbf{C}_d$ is the a priori covariance matrix, $\mathbf{m}_0$ is the reference model, $\mathbf{C}_m$ is the a priori model covariance matrix, $\mathbf{D}$ is the second derivative smoothing operator and ϵ is referred to as the *damping* factor and η as the *smoothing* factor (Rawlinson et al., 2006). According to the subspace scheme, the perturbation δm required to minimise the objective function defined in Equation 2 is:

$$\delta \mathbf{m} = -\mathbf{A}[\mathbf{A}^T(\mathbf{G}^T \mathbf{C}_d^{-1} \mathbf{G} + \epsilon \mathbf{C}_m^{-1} + \eta \mathbf{D}^T \mathbf{D})\mathbf{A}]^{-1} \mathbf{A}^T \hat{\gamma} \quad (3)$$

where, $\mathbf{A} = [a^j]$ is the $M \times n$ projection matrix (built from the gradient vector and its rates of change), $\mathbf{G}$ is the matrix of Frêchet derivatives and $\hat{\gamma}$ is the gradient vector ($\hat{\gamma} = \frac{\partial S}{\partial \mathbf{m}}$). For more details on the subspace inversion scheme, see Rawlinson and Sambridge (2003); Rawlinson et al. (2006). In order to represent structure, FMTOMO uses cubic B-splines to describe continuous velocity variations from the 3-D model parameter grid; similarly, continuous interfaces such as the Moho are described by applying cubic B-splines to a 2-D interface grid. Further details on FMTOMO can be found in de Kool et al. (2006) and Rawlinson et al. (2006).

We choose to describe our model in terms of a crust and a mantle layer separated by the Moho interface, which is defined by the crust1.0 global model of Laske et al. (2013). The 1-D ak135 reference model was not found to be ideal for a starting model in the mantle, since it produced largely positive velocity models below 300 km depth following the inversion. Instead, we have produced a reference 1-D model using FMTOMO in what is effectively a 1-D inversion mode (see Figure ~~S2~~S3). The grid spacing of the final ~~3D~~ 3-D models was set to 1.2° ~~and~~ in latitude and longitude for P-wave model, 2° ~~horizontally and~~ in latitude and longitude for S-wave model and 55 km vertically for both P- and S-wave models respectively. The crustal part of the model was more densely parametrised, leading to a ~~resolution~~ minimum permitted structural scale-length of approximately 0.5° horizontally and 16 km vertically. We obtained different 3-D models of the region based on the four sets of earthquake locations, as described above. For P-wave tomography, we compared results obtained from models P_A, P_B, P_C and P_D (Table 1). The ~~3D~~ 3-D P- and S-wave tomographic models obtained with the ISC-EHB dataset (Figures 6, 10) show a ~~reduction of data variance~~ data variance reduction of 63.1% for Vp and 42.8% for Vs, which equates to a final RMS misfit of 681 ms for Vp and 704 ms for Vs.

4. Results

4.1. Stability and resolution of the results

Our dataset of regional ~~travel times~~ travel-times was inverted for both velocity variations and interface depth. We analysed the relationship between data variance, model variance and model roughness to obtain the best damping (ϵ) and smoothing (η) parameters. We encountered the same issue as Pesicek et al. (2010), who observed that determining the regularising parameters solely from synthetic tests produces models that are underdamped. This underdamping occurs because synthetic tests cannot represent the true noise in the dataset. We instead use a hybrid approach based on both model results (as sometimes used in global tomography~~(Pesicek et al., 2010)~~, e.g. Pesicek et al. (2010)) and trade-off curves (from real and synthetic data) to choose the optimum smoothing and damping (See Figures ~~S3,~~ S4, S5, S6, S7, S8, S9~~and~~ , S10 and S11). In some applications of global tomography the optimum regularisation parameters are obtained when the model best recovers the velocity anomalies that are associated with known geological features (e.g. subduction zones), while with trade-off tests, optimum regularisation occurs at or near the point of maximum curvature.

We performed a synthetic checkerboard test that includes the addition of Gaussian noise with a standard deviation of 0.5 s to the synthetic ~~travel times~~ travel-times in order to simulate the arrival time picking uncertainty. The new ~~travel times~~ travel-times serve as the synthetic observables in the inversion. The test is done for three different checkerboard sizes (noting that the S-wave checkerboard anomalies are larger than the corresponding P-wave checkerboard anomalies in each of the three cases owing to much reduced data coverage). The checkerboard sizes for P-wave are: 2° horizontally and 80 km vertically for the coarse grid, 1.2° horizontally and 53 km vertically for the medium grid and 0.75° and 40 km vertically for the fine grid and for S-wave: 3° horizontally 80 km for the coarse grid, 2.2° horizontally and 80 km for the medium grid and 1.2° horizontally and 53 km vertically for the fine grid. The robustness of the solution depends on path coverage and data noise. Checkerboard anomalies were recovered using the same source-receiver paths corresponding to the observables and the same input parameters. The best checkerboard recovery occurs in the Philippines, Sulawesi and along the Sunda arc (see Figure 4). A gap in station distribution across the South China Sea reduces resolution in this region of the model. In general, the coarser checkerboard is better ~~resolved~~ recovered over a larger region compared to the finer checkerboard~~, which is to be expected~~. Cross sections through the checkerboard are shown in Figures ~~S11,~~ S12, S13, S14, S15 and reveal that good resolution can be achieved down to about 800 km depth, although the well-recovered areas tend to decrease as depth increases due to the raypath geometry. The S-wave checkerboard tests ~~, in general,~~ indicate that the minimum size of the recovered anomalies is larger ~~compared to the P-wave results, which is to be expected due to the much smaller size of the~~ than for P-waves; this is expected, as the S-wave ~~dataset (see Figure 5)~~dataset is significantly smaller. While we do not account for finite frequency effects in our tomography, it is also worth noting that S-waves are typically comprised of longer-period signals, increasing the width of the corresponding sensitivity kernels (Tian et al., 2009). Typically longer wavelength structure ought to be better recovered compared to shorter wavelength structure in the presence of sparse ray coverage.

[Figure 4 Checkerboard P]

[Figure 5 Checkerboard S]

4.2. *Tomographic models with different datasets*

We seek to test the robustness of our results with respect to the input observables. Different catalogues have different sources, different source locations and different picks. If we test a variety of different datasets and find that similar features emerge, then we can be more confident that they are not artefacts resulting from a particular choice of catalogue. We also test the effect of including crustal phases and different crustal models. All these models are summarised in Table 1. The P-wave tomographic models (P_A, P_B, P_C, P_D) can be compared in Figures 6 and 7 at depths of 200 km and 300 km, respectively. Figure 6 reveals some clear differences between the four models in a number of regions including the Sunda-Banda arc and Sulawesi region (Figure 1). In particular, the aforementioned regions appear to be better reconstructed when using NLL-ISC-EHB (P_B) and NLL-ISC-Reviewed (P_D) because these models more closely resemble the results from previous studies and reveal known geological features. At greater depths (see Figure 7) the differences between the models are less pronounced in the well-resolved regions.

[Figure 6 P 200]

[Figure 7 P 300]

The P-wave tomographic models show multiple high wave-speed anomalies marking subducting slabs in the SE-Asia upper mantle (Figures 6-7). One of the best resolved high wave-speed anomalies is along the Sunda-Java arc (Figure 1), where the Indo-Australian plate subducts below the Sundaland plate. This is depicted with a high velocity anomaly which shifts towards Borneo as the depth increases (Figure 8ii). Subduction associated with the Sunda arc extends eastwards until the Banda arc. The horseshoe-shaped high-velocity anomaly beneath Banda (Puspito et al., 1993) is evident in Figure 6 while Figure 7 shows a spoon-shaped slab with a flat lying portion beneath the Banda Sea. The final models also show the Philippine trench and Sangihe-Halmahera arc-arc subduction near Sulawesi (Figure 8) as localised high velocity zones. That all of these features are largely consistent across the model ensemble is supported by the votemap we illustrate in Figure 9.

[Figure 8 P cross]

[Figure 9 Votemap]

In the case of S-waves, due to the reduced size of the dataset compared to P-waves, we decided to only use ISC-EHB, for which we produced four results (S_A, S_B, S_C, S_D as shown in Table 1). The rest of the datasets were not used for different reasons. ISC-Reviewed is a poorer quality dataset compared to ISC-EHB and datasets produced by NLL would contain less data since we require more than 40 arrivals with RMS less than 10s, as described above, which may result in the loss of important arrivals. This NLL approach is entirely automatic and unsupervised i.e. no manual “grooming” was done by analysts as it was the case of ISC-EHB. We don’t have complete information on these methods, which are often based on heavily-supervised approaches; as an example, for the ISC-EHB catalogue, reassign the depth of some events based on other sources of information. In particular, they plot together the newly relocated and ISC-GEM (Storchak et al., 2015) events along the subduction zones taking into account their curvature and use these plots to confirm or modify the earthquakes’ depth. This difference between the two approaches reduces the number of arrivals produced by NLL significantly enough, not to consider them for S-wave tomography. The S-wave tomographic model (S_A), in which only mantle velocity structures are inverted for, is shown in Figure 10. The S-wave models are obtained using a dataset that is approximately 21% (comparing ISC-EHB datasets i.e. P_E with S_A) the size of the P-wave dataset (Table 1), resulting in a lower-resolution model (see Figure 10). This difference in resolution makes it difficult to compare the P- and S-wave models directly, although ostensibly the broad scale features of the two models are quite similar. Figure 11 does exhibit notable differences from Figure 8, in particular the cross-sections i, ii, iv and v. In Figure 11ii we see no evidence of continuous subduction beneath Java and the small aseismic region in the slab east of Java, which is interpreted as a hole by Hall and Spakman (2015) does not correspond to a S-wave velocity anomaly in Figure 11iv. Finally, the inverted U-shaped arc-arc collision in northeastern Sulawesi shows a high S-wavespeed anomaly in the Halmahera slab extending down to 500 km as seen in Figure 11v.

[Figure ~~9~~ 10 S-wave] [Figure ~~10~~ 11 S cross]

Perturbations in P-wavespeed and S-wavespeed crustal structure, relative to the crust1.0 starting model (P_E, S_B), are shown in Figure ~~S15~~S16; in this example, we have allowed crustal velocity to be constrained in addition to mantle velocity to examine to what extent variations in crustal velocities might influence the recovery of mantle structure. A negative velocity anomaly is shown beneath the Sunda arc in both models. In contrast, a positive velocity anomaly is shown beneath the Philippines in the P-wave model while a negative anomaly is shown in the S-wave model. Similar results are shown in Figure ~~S16~~ S17 where the global model ak135 was used as a starting model (P_G, S_D). Models P_F and S_C include crustal phases in the inversion, but they do not show velocity differences from the models P_E and S_B because the number of the Pg/Sg and Pb/Sb phases is small compared to the full dataset. In addition, we have investigated how the mantle velocity model is affected when inverting for both crust and mantle (see Figures 8 and ~~S17~~S19) by comparing models P_D and P_H. In all our models we also invert for the Moho interface geometry~~, however~~; however, we observe no notable differences from the starting interface we adopt from crust1.0.

4.3. Discussion

Overall, the NLL-selected dataset and ISC-EHB catalogues appear to give better results than the ISC-Reviewed catalogue. This is expected since the ISC reviewing process only requires that the depth of the event is appropriate for the region in which it occurs and checks for outliers and ~~mis-associated~~ incorrectly associated phases. On the other hand, the NLL and ISC-EHB catalogue perform a relocation of the ISC events (and dynamic phase identification ~~for~~ in the case of ISC-EHB) (Bondár and Storchak, 2011; Engdahl et al., 1998). ~~A~~ The votemaps for the models P_A, P_B, P_C, P_D are shown in Figures 9 and S18. These two figures reveal regions of the model in which we can be more confident that velocity anomalies exist. In general, all our models agree on the basic pattern of velocity anomalies. A comparison between our P_D model and Amaru (2007) can be seen in Figure ~~S18~~ S20 which shows that both models exhibit similar features. Votemaps have only been produced for models P_A, P_B, P_C, P_D which occur from different datasets. Votemaps for S-wave models were not produced since we use the same dataset which does not lead to major changes in mantle velocities. The model of Amaru (2007) is a global model constrained by 18 million P-wave picks and uses adaptive parametrisation to deal with irregular data distribution. In our models, we explicitly include a crustal layer and invert for S-wave as well as P-wave velocity anomalies using regional sources only. We have also adopted a different approach for the ~~travel time~~ travel-time prediction and inversion, based on ~~FMM~~FMTOMO, NLL and the incorporation of crust1.0 (rather than its predecessor crust2.0) - we also include inversion for crustal velocity and Moho depth. This allows specific inclusion of Pb/Sb and Pg/Sg crustal phases which further refine crustal structure. Moreover, we have adopted a new machine-learning clustering approach for similar creating summary rays from raypaths which improved the S/N ratio and reduced the number of data~~and as a result, it removed much of the data inconsistencies~~ ; as a consequence, data inconsistencies have been removed or suppressed. As seen in Figure ~~S1~~ S2 the noise in the data prior to signal ~~improvement~~ enhancement reduced the quality of the results and blurred known geological features such as the arc-arc collision in the Sulawesi region. The high quality P-wave models produced are in general agreement with the Slab2 subduction geometry model (Hayes et al., 2018) especially in the Sulawesi region which features a complex subduction system. Our S-wave model is the first of its kind for southeast Asia, and therefore comparison with pre-existing S-wave models, such as the one derived from surface wave tomography by Lebedev and Nolet (2003) is not straighforward. Having both P- and S-wave tomographic models has the potential to yield greater insight into the geological structure and plate tectonic evolution of the region. Here, we interpret the two models (P_D,S_A) that were obtained using what we regard as the best datasets available, but the primary features we interpret are also present in the other models.

4.3.1. *Sundaland core*

All P-wave and S-wave models produced in this study exhibit low velocity anomalies between 100-200 km depth in the region encompassed by the Thai-Malay Peninsula, Borneo, Java Sea and Sunda Shelf, as can be seen from Figures 6, 9 and 10. This region is part of the Sundaland continent, which is mostly composed of continental fragments added to Asia during the Triassic to Cretaceous periods (Hall and Morley, 2004; Hall, 2012; Metcalfe, 2011, 2013; Hall and Spakman, 2015). All our models thus point to the presence of the same weakened thermal continental lithosphere inferred by previous studies (Hafkenscheid et al., 2001; Lebedev and Nolet, 2003; Replumaz et al., 2004; Hall and Spakman, 2015). This thermal weakening might have occurred from long-term Cenozoic subduction, plumes, or be the result of the interaction between Triassic and Cretaceous continental blocks (Hall and Spakman, 2015).

4.3.2. *Sumatra and Java*

~~The~~ Figures 8i and 11i show that the western part of the slab under Sumatra dips north at about 20°, progressively increasing in depth while moving northeastward. The P- and S-wave models differ slightly between 300 km and 400 km depth, especially between Sumatra and Java (compare Figures 8i and 11i). Both P- and S-wave models show a major break in the high-velocity slab structure; this contrasts with the P-wave velocity model ~~(Hall and Spakman, 2015)~~ of Hall and Spakman (2015) in which the high velocity slab extends continuously in depth. One possible explanation that is consistent with this observation is the presence of increased temperatures at a depth of around 350 km, which may contribute to the intense volcanism affecting the region. Fukao et al. (1992) suggested that the Java slab dips steeply in the lower part of the upper mantle and proposed a mechanism based on thickened and buckled subducted slab forming a megalith, which penetrated into the lower mantle due to its high density. This is depicted in Figure 8ii; however, we also observe a thinning of the subducted lithosphere at approximately 400 km depth. In contrast, we do not observe the slab in Figure 11ii where ~~probably~~ the thickness of the subducting slab likely drops below the resolving power of the S-wave dataset at this depth. The absence of intense seismicity at this depth supports an argument of slab spreading with a possible tear. Both P- and S-wave models provide evidence for serpentinisation at 100 km below central Java as seen in Figures 8ii and 11ii, with a low velocity anomaly and absence of seismicity in the mantle wedge.

Both P- and S-wave tomographic models show a hole in the slab in Figures 8iii and 11iii between depths of 350 and 500 km in East Java. The hole observed in both the P and S-wave models points to a temperature increase influencing the velocity of the waves and supports the interpretation of Hall and Spakman (2015). They suggested that this aseismic, low-velocity anomaly was produced by an object blocking the slab during Late Miocene subduction, thus producing a tear. However, the second smaller hole in the slab east of Java is not imaged in the S-wave model, possibly due to the size of the hole (150 km) being ~~lower~~ smaller than the resolution of the S-wave model (220 km). In Figure 11vi we show a ~~section~~ cross-section approximatevely parallel to ~~subduction~~the subduction zone. Beneath Sumbawa, a low-velocity aseismic anomaly below 100 km depth may be evidence of serpentinisation as seen in Figure 11iv. Serpentinisation most commonly occurs at the plate boundaries where water is released from the descending oceanic crust and absorbed by the adjacent mantle peridotite (Cheng et al., 2012).

The tear or fold ~~of~~ in the slab beneath North Sumatra is imaged in both P- and S-wave models in Figures 7 and 10, and is most obviously observed at around 300 km depth. The difference between P- and S-wave models is most evident in Figures 8v and 11v; here, the S-wave model shows no evidence of high wave-speed subducted lithosphere starting at approximately 300 km depth, as seen in the western portion of the P-wave velocity cross-section. One possible reason for the lack of this deeper high velocity anomaly in the S-wave model is a lack of resolution (it is at the limit of what the S-wave checkerboard test can resolve), although it may also due be to the smearing of P-waves (although the P-wave checkerboard tests do not suggest that much smearing is present).

4.3.3. Banda arc

Puspito et al. (1993) imaged the Banda arc subduction zone as a horseshoe-shaped positive wave speed anomaly. This ~~featured is~~ feature is also visible in our P-wave model (Figure 6). The eastern portion of Figure 8vi shows west-dipping subduction with intense seismicity, supporting the observation of Puspito et al. (1993) of a curved subduction zone. The subducting slab in the Banda region reaches the bottom of the upper mantle ($\sim$700 km depth). Puspito and Shimazaki (1995) concluded that this slab does not penetrate into the lower mantle, in contrast to the western subduction zone along the Sunda-Java arc. The tomographic models of Widiyantoro and van der Hilst (1996) and Widiyantoro and van der Hilst (1997) show a laterally-continuous subduction along the Sunda-Banda arc and north under the Molucca Sea (~~Figure 6~~Figures 6, 9). In their full waveform tomography, Fichtner et al. (2010) show a high-velocity S-wave anomaly below Timor at 200 km depth, which is consistent with that retrieved in our S_A model (Figure. 10). The anomaly suggests lower temperatures extending from North Australia to the Banda Sea. This positive velocity anomaly between 100 km and 200 km depth is consistent with the thickness of ~~the expected~~ Australian Precambrian lithosphere as interpreted by Fichtner et al. (2010) using the correlation of isotope signatures and tomographic images. The aforementioned two models agree on the geometry of the subduction zone with an almost vertical subduction of the Australian lithosphere beneath Sumba, as seen in Figures 8iv and 11iv, at least for the first 350 km.

4.3.4. Sulawesi and Borneo

Puspito et al. (1993) proposed that the western limb (Sangihe slab) of the Molucca Sea plate may penetrate into the lower mantle in contrast to the eastern limb (Halmahera slab), which only reaches depths of approximately 400 km. This is confirmed from our study as shown in Figure 8v, where the Sangihe slab reaches depths of approximately 700 km while the Halmahera slab is shown to terminate at 400 km depth. In contrast to the P-wave modelling results, the S-wave model in Figure 11v shows that the eastern dipping slab (Halmahera) reaches depths of 500 km although this difference may be due to the more limited resolving power of the S-wave dataset.

In the northern part of Borneo we observe (Figures 6, 7, 8iii, 10 and 11iii) a high velocity anomaly between 100-300 km depth which is also observed by Hall and Spakman (2015). They suggest that the anomaly might be an artefact of the poor data coverage, but it is present in both P-wave and S-wave models and appears to be resolved according to our synthetic resolution tests. The absence of seismicity in the area suggests that this anomaly might be an indication of possible remnant subduction; for instance, both Cottam et al. (2013) and Hall (2013) suggest that the anomaly may represent a broken off part of the slab from northerly subduction of the Celebes Sea in the mid-late Miocene, which terminated only 5 Ma. Alternatively, it could be related to subduction termination of the South China Sea in the mid-Miocene when the Dangerous Grounds block collided with the Sabah-Cagayan volcanic arc (Cottam et al., 2013). The lithospheric thickness below Borneo is estimated to be around 100 km based on the depth of the P- and S-wave velocity ~~increase~~ decrease observed in Figures 8iii and 11iii.

5. Conclusions

We have developed 12 tomographic models in total, with the aim of providing a robust and consistent picture of the upper-mid mantle beneath SE Asia. These 12 models include eight ~~P-~~ P-wave and four S-wave models which were produced using an iterative non-linear inversion scheme in which FMM was used for ~~travel time~~ travel-time prediction and a subspace inversion scheme for adjusting model parameters in order to satisfy observations. This method was used to constrain the 3-D seismic structure of SE Asia with four datasets and different starting models. We incorporated the crust1.0 model to minimise the downward smearing of crustal structure in order to improve the mantle model and have examined the influence of inverting for crustal structure using phases such as Pg. Moreover, we generated new S-wave tomographic models, which provide fresh insight into the subduction processes taking place in the collision zone.

Based on the results of this study, we conclude that using the NLL locations and ISC-EHB catalogue in the inversion produced better P-wave models compared to using the default catalogue locations. ~~The~~ Inversion of the S-wave dataset resulted in a model that was comparable to a smoothed version of the P-wave model although there were a number of clear differences in the Sulawesi and Java regions. In particular, all models agree that in the region of the Thai-Malay Peninsula, Borneo, Java Sea and Sunda Shelf low-velocity anomalies suggest thermal weakening of the continental lithosphere. In addition, we confirm that the subducting slab below Java dips steeply in the upper part of the lower mantle, with a possible thinning of the subducted lithosphere at approximately 400 km depth. This feature is confirmed in the S-wave model, where we can see no evidence of subduction possibly due to the reduced resolution. Moreover, both the P-wave and S-wave models show that the Sangihe slab of the Molucca Sea may penetrate into the lower mantle while the Halmahera slab reaches a depth of only 400-500 km. A hole in the slab beneath East Java is apparent in both the P-wave and S-wave models. It is likely due to an absence of cold lithosphere caused by a tear, which explains the lower wavespeeds observed in both P- and S-wavespeeds. A smaller hole is located to the east of this hole in the P-wave model but is not visible in the S-wave model. Finally, we observed a consistent high velocity anomaly beneath North Borneo, reaching 300 km depth, which may be a signature of remnant subduction related to recent subduction termination (5 Ma) in the northern Celebes Sea.

References

Amaru, M.L., 2007. Global travel time tomography with 3-D reference models. Geologica Ultraiectina 274, 1–174.

Bijwaard, H., Spakman, W., Engdahl, E.R., 1998. Closing the gap between regional and global travel time tomography. Journal of Geophysical Research: Solid Earth 103, 30055–30078.

Bird, P., 2003. An updated digital model of plate boundaries. Geochemistry, Geophysics, Geosystems 4.

Bondár, I., Storchak, D., 2011. Improved location procedures at the International Seismological Centre. Geophysical Journal International 186, 1220–1244.

Cardwell, R.K., Isacks, B.L., 1978. Geometry of the subducted lithosphere beneath the Banda Sea in eastern Indonesia from seismicity and fault plane solutions. Journal of Geophysical Research: Solid Earth 83, 2825–2838.

Charlton, T.R., 2000. Tertiary evolution of the eastern Indonesia collision complex. Journal of Asian Earth Sciences 18, 603–631.

Cheng, W.B., Hsu, S.K., Chang, C.H., 2012. Tomography of the southern Taiwan subduction zone and possible emplacement of crustal rocks into the forearc mantle. Global and Planetary Change 90-91, 20–28.

Cottam, M.A., Hall, R., Sperber, C., Kohn, B.P., Forster, M.A., Batt, G.E., 2013. Neogene rock uplift and erosion in northern Borneo: evidence from the Kinabalu granite, Mount Kinabalu. Journal of the Geological Society 170, 805–816.

Daruru, S., Dhandapani, S., Gupta, G., Iliev, I., Xu, W., Navratil, P., Marín, N., Ghosh, J., 2010. Distributed, scalable clustering for detecting halos in terascale astronomy datasets. Proceedings - IEEE International Conference on Data Mining, ICDM , 138–147.

Das, S., 2004. Seismicity gaps and the shape of the seismic zone in the Banda Sea region from relocated hypocenters. Journal of Geophysical Research: Solid Earth 109, B12303.

Engdahl, E.R., Gunst, R.H., 1966. Use of a high speed computer for the preliminary determination of earthquake hypocenters. Bull. Seismol. Soc. Am. 56, 325–336.

Engdahl, E.R., Van Hilst, R.D., Buland, R., 1998. Global teleseismic earthquake relocation with improved travel times and procedures for depth determination. Bulletin of the Seismological Society of America 88, 722–743.

Ester, M., Kriegel, H.P., Sander, J., Xu, X., 1996. A Density-Based Algorithm for Discovering Clusters in Large Spatial Databases with Noise. In: Proceedings of the 2nd International Conference on Knowledge Discovery and Data Mining, Portland , 226–23110.1.1.71.1980.

Fichtner, A., De Wit, M., van Bergen, M., 2010. Subduction of continental lithosphere in the Banda Sea region: Combining evidence from full waveform tomography and isotope ratios. Earth and Planetary Science Letters 297, 405–412.

Fukao, Y., Obayashi, M., Inoue, H., Nenbai, M., 1992. Subducting slabs stagnant in the mantle transition zone. Journal of Geophysical Research 97, 4809–4822.

Goes, S., Govers, R., Vacher, P., 2000. Shallow mantle temperatures under Europe from P and S wave tomography. Journal of Geophysical Research: Solid Earth 105, 11153–11169.

Gudmundsson, O., Davies, J.H., Clayton, R.W., 1990. Stochastic analysis of global travel time data: Mantle heterogeneity and random errors in the ISC data. Geophysical Journal International 102, 25–43.

Hafkenscheid, E., Buiter, S.J.H., Wortel, M.J.R., Spakman, W., Bijwaard, H., 2001. Modelling the seismic velocity structure beneath Indonesia: A comparison with tomography. Tectonophysics 333, 35–46.

Hall, R., 1997. Cenozoic tectonics of SE Asia and Australasia, in: Petroleum Systems of SE Asia and Australia, pp. 155–170.

Hall, R., 2009. Hydrocarbon basins in SE Asia: understanding why they are there. Petroleum Geoscience 15, 131–146.

Hall, R., 2012. Late Jurassic–Cenozoic reconstructions of the Indonesian region and the Indian Ocean. Tectonophysics 570, 1–41.

Hall, R., 2013. Contraction and extension in northern Borneo driven by subduction rollback. Journal of Asian Earth Sciences 76, 399–411.

Hall, R., Morley, C.K., 2004. Sundaland basins. Geophysical Monograph Series 149, 55–85.

Hall, R., Spakman, W., 2015. Mantle structure and tectonic history of SE Asia. Tectonophysics 658, 14–45.

Hamilton, W.B., 1974. Earthquake map of the Indonesian Region. U.S. Geological Survey, Miscellaneous Investigations Series Map .

Hamilton, W.B., 1979. Tectonics of the Indonesian Region. geological survey , 352.

Hatherton, T., Dickinson, W.R., 1969. The relationship between andesitic volcanism and seismicity in Indonesia, the Lesser Antilles, and other island arcs. Journal of Geophysical Research 74, 5301–5309.

Hayes, G.P., Moore, G.L., Portner, D.E., Hearne, M., Flamme, H., Furtney, M., Smoczyk, G.M., 2018. Slab2, a comprehensive subduction zone geometry model. Science 362, 58–61.

Kennett, B.L.N., Engdahl, E.R., Buland, R., 1995. Constraints on seismic velocities in the Earth from travel times. Geophysical Journal International 122, 108–124.

Kennett, B.L.N., Sambridge, M.S., Williamson, P.R., 1988. Subspace methods for large inverse problems with multiple parameter classes. Geophysical Journal International 94, 237–247.

de Kool, M., Rawlinson, N., Sambridge, M., 2006. A practical grid-based method for tracking multiple refraction and reflection phases in three-dimensional heterogeneous media. Geophysical Journal International 167, 253–270.

Kopp, H., Flueh, E.R., Petersen, C.J., Weinrebe, W., Wittwer, A., Scientists, M., 2006. The Java margin revisited: Evidence for subduction erosion off Java. Earth and Planetary Science Letters 242, 130–142.

Laske, G., Masters, G., Ma, Z., Pasyanos, M., 2013. Update on CRUST1.0—A 1-degree global model of Earth's crust. EGU General Assembly 2013 15, 2658.

Lebedev, S., Nolet, G., 2003. Upper mantle beneath Southeast Asia from S velocity tomography. J. Geophys. Res. 108, 2048.

Lomax, A., Curtis, A., 2001. Tutorial Prior information , sampling distributions , and the curse of dimensionality. Geophysics 66, 372 – 378.

Lomax, A., Michelini, A., Curtis, A., 2009. Earthquake Location, Direct, Global-Search Methods. Complexity In Encyclopedia of Complexity and System Science, Part 5 , 2449–2473.

Lomax, A., Zollo, A., Capuano, P., Virieux, J., 2001. Precise, absolute earthquake location under Somma-Vesuvius volcano using a new three-dimensional velocity model. Geophysical Journal International 146, 313–331.

Metcalfe, I., 2013. Gondwana dispersion and Asian accretion: Tectonic and palaeogeographic evolution of eastern Tethys. Journal of Asian Earth Sciences 66, 1–33.

Metcalfe, I.a.N., 2011. Palaeozoic Mesozoic history of SE Asia. Geological Society, London, Special Publications , 7–35.

Milsom, J., 2001. Subduction in eastern Indonesia: How many slabs? Tectonophysics 338, 167–178.

Pedregosa, F., Varoquaux, G., Gramfort, A., Michel, V., Thirion, B., Grisel, O., Blondel, M., Prettenhofer, P., Weiss, R., Dubourg, V., Vanderplas, J., Passos, A., Cournapeau, D., Brucher, M., Perrot, M., Duchesnay, É., 2012. Scikit-learn: Machine Learning in Python. Journal of Machine Learning Research 12, 2825–2830. 1201.0490.

Pesicek, J.D., Thurber, C.H., Widiyantoro, S., Engdahl, E.R., DeShon, H.R., 2008. Complex slab subduction beneath northern Sumatra. Geophysical Research Letters 35, 1–5.

Pesicek, J.D., Thurber, C.H., Widiyantoro, S., Zhang, H., DeShon, H.R., Engdahl, E.R., 2010. Sharpening the tomographic image of the subducting slab below Sumatra, the Andaman Islands and Burma. Geophysical Journal International 182, 433–453.

Puspito, N.T., Shimazaki, K., 1995. Mantle structure and seismotectonics of the Sunda and Banda arcs. Tectonophysics 251, 215–228.

Puspito, N.T., Yamanaka, Y., Miyatake, T., Shimazaki, K., Hirahara, K., 1993. Three-dimensional P-wave velocity structure beneath the Indonesian region. Tectonophysics 220, 175–192.

Pyrcz, M.J., Deutsch, C.V., 2002. Declustering and Debiasing. Technical Report January 2007. University of Alberta.

Rawlinson, N., Hauser, J., Sambridge, M., 2008. Seismic ray tracing and wavefront tracking in laterally heterogeneous media. Advances in Geophysics 49, 203–273.

Rawlinson, N., Reading, A.M., Kennett, B.L., 2006. Lithospheric structure of Tasmania from a novel form of teleseismic tomography. Journal of Geophysical Research: Solid Earth 111, 1–21.

Rawlinson, N., Sambridge, M., 2003. Seismic Traveltime Tomography of the Crust and Lithosphere. Advances in Geophysics 46, 81–198.

Rawlinson, N., Sambridge, M., 2004a. Multiple reflection and transmission phases in complex layered media using a multistage fast marching method. Geophysics 69, 1338–1350.

Rawlinson, N., Sambridge, M., 2004b. Wave front evolution in strongly heterogeneous layered media using the fast marching method. Geophysical Journal International 156, 631–647.

Replumaz, A., Kárason, H., van der Hilst, R.D., Besse, J., Tapponnier, P., 2004. 4-D evolution of SE Asia's mantle from geological reconstructions and seismic tomography. Earth and Planetary Science Letters 221, 103–115.

Sethian, J.A., 1996. A fast marching level set method for monotonically advancing fronts. Proceedings of the National Academy of Sciences 93, 1591–1595.

Sethian, J.A., Popovici, A.M., 1999. 3-D traveltime computation using the fast marching method. Geophysics 64, 516–523.

Simandjuntak, T.O., Barber, A.J., 1996. Contrasting tectonic styles in the Neogene orogenic belts of Indonesia. Geological Society, London, Special Publications 106, 185–201.

Spakman, W., Hall, R., 2010. Surface deformation and slabmantle interaction during Banda arc subduction rollback. Nature Geoscience 3, 562–566.

Storchak, D.A., Di Giacomo, D., Engdahl, E.R., Harris, J., Bondár, I., Lee, W.H., Bormann, P., Villaseñor, A., 2015. The ISC-GEM Global Instrumental Earthquake Catalogue (1900-2009): Introduction. Physics of the Earth and Planetary Interiors 239, 48–63.

Tian, Y., Sigloch, K., Nolet, G., 2009. Multiple-frequency SH-wave tomography of the western US upper mantle.

Geophysical Journal International 178, 1384–1402.

Trampert, J., Vacher, P., Vlaar, N., 2001. Sensitivities of seismic velocities to temperature, pressure and composition in the lower mantle. Physics of the Earth and Planetary Interiors 124, 255–267.

Weston, J., Engdahl, E.R., Harris, J., Di Giacomo, D., Storchak, D.A., 2018. ISC-EHB: Reconstruction of a robust earthquake data set. Geophysical Journal International 214, 474–484.

Widiyantoro, S., van der Hilst, R.D., 1996. Structure and Evolution of Lithospheric Slab. Science 271, 1566–1570.

Widiyantoro, S., van der Hilst, R.D., 1997. Mantle structure beneath Indonesia infered from high-resolution tomography imaging. Geophys. J. Int. 130, 167–182.

Widiyantoro, S., Pesicek, J.D., Thurber, C.H., 2011. Subducting slab structure below the eastern Sunda arc inferred from non-linear seismic tomographic imaging. Geological Society, London, Special Publications 355, 139–155.

Zenonos, A., Stein, S., Jennings, N.R., 2018. Coordinating Measurements in Uncertain Participatory Sensing Settings. Journal of Artificial Intelligence Research 61, 433–474.

Table 1: A summary of the characteristics of the tomographic models generated as part of this study.

Model name	**Dataset**	**No. of picks**	**Starting model (crust/mantle)**	**Inverting for**
P_A	ISC-EHB-R	219592	crust1.0/ak135	mantle
P_B	NLL-ISC-EHB	263662	crust1.0/ak135	mantle
P_C	ISC-Reviewed-R	266696	crust1.0/ak135	mantle
P_D	NLL-ISC-Reviewed	309964	crust1.0/ak135	mantle
P_E	ISC-EHB	444514	crust1.0/ak135	crust/mantle
P_F	ISC-EHB with Pg, Pb	446785	crust1.0/ak135	crust/mantle
P_G	ISC-EHB	444514	ak135/ak135	crust/mantle
P_H	NLL-ISC-Reviewed	309964	crust1.0/ak135	crust/mantle
S_A	ISC-EHB	93850	crust1.0/ak135	mantle
S_B	ISC-EHB	93850	crust1.0/ak135	crust/mantle
S_C	ISC-EHB with ~~Pg, Pb~~ Sg, Sb	96975	crust1.0/ak135	crust/mantle
S_D	ISC-EHB	93850	ak135/ak135	crust/mantle

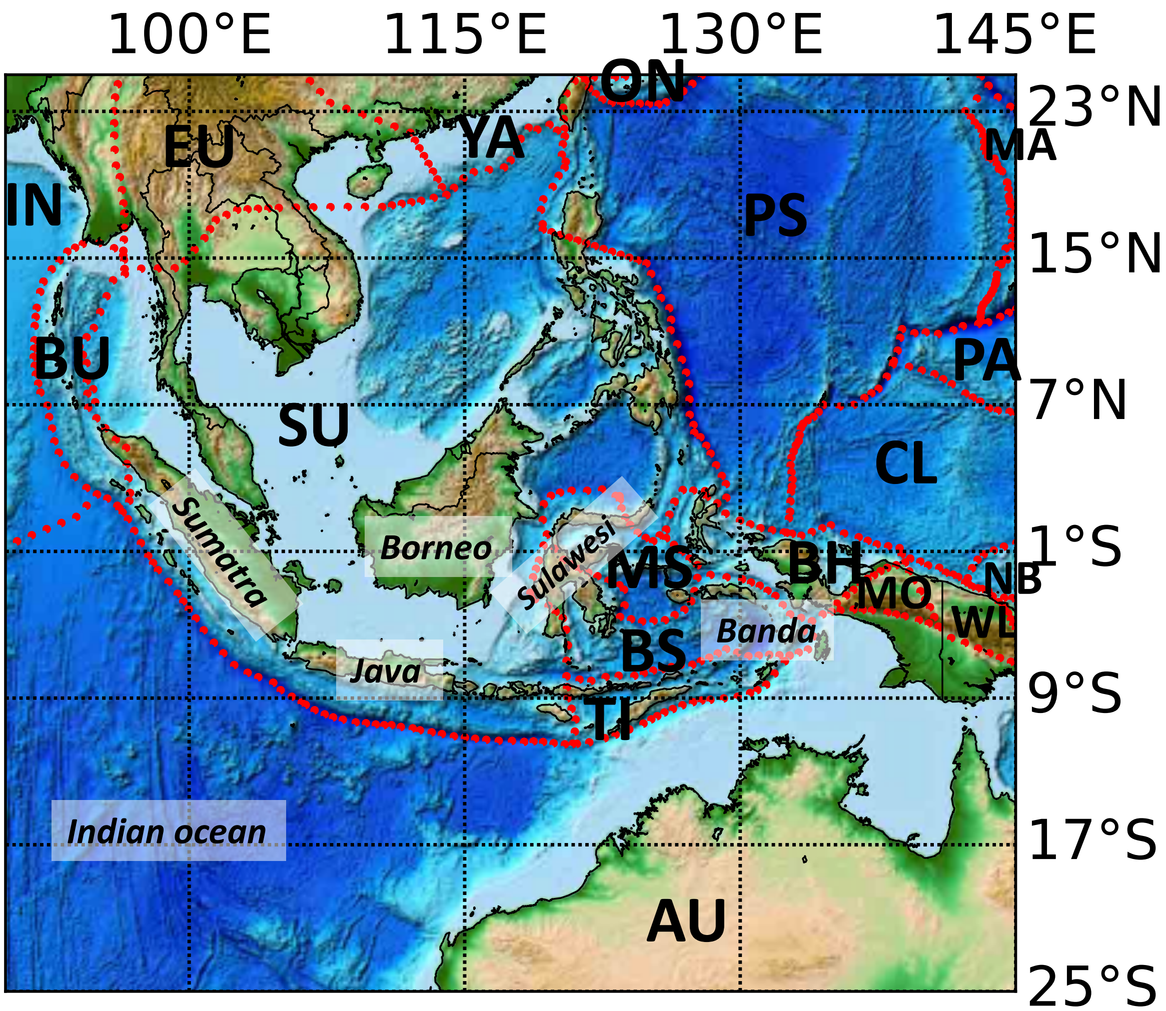

Figure 1: Plate boundaries of SE Asia as interpreted by Bird (2003). The tectonic plates which are labelled include, AU: Australia, BH: Birds Head, BS: Band Sea, BU: Burma, CL: Caroline, EU: Eurasia, IN: India, MA: Mariana, MO: Maoke, MS: Molucca Sea, NB: North Bismarck, ON: Okinawa, PA: Pacific, PS: Philippine Sea, SU: Sunda, TI: Timor, WL: Woodlark, YA: Yangtze.

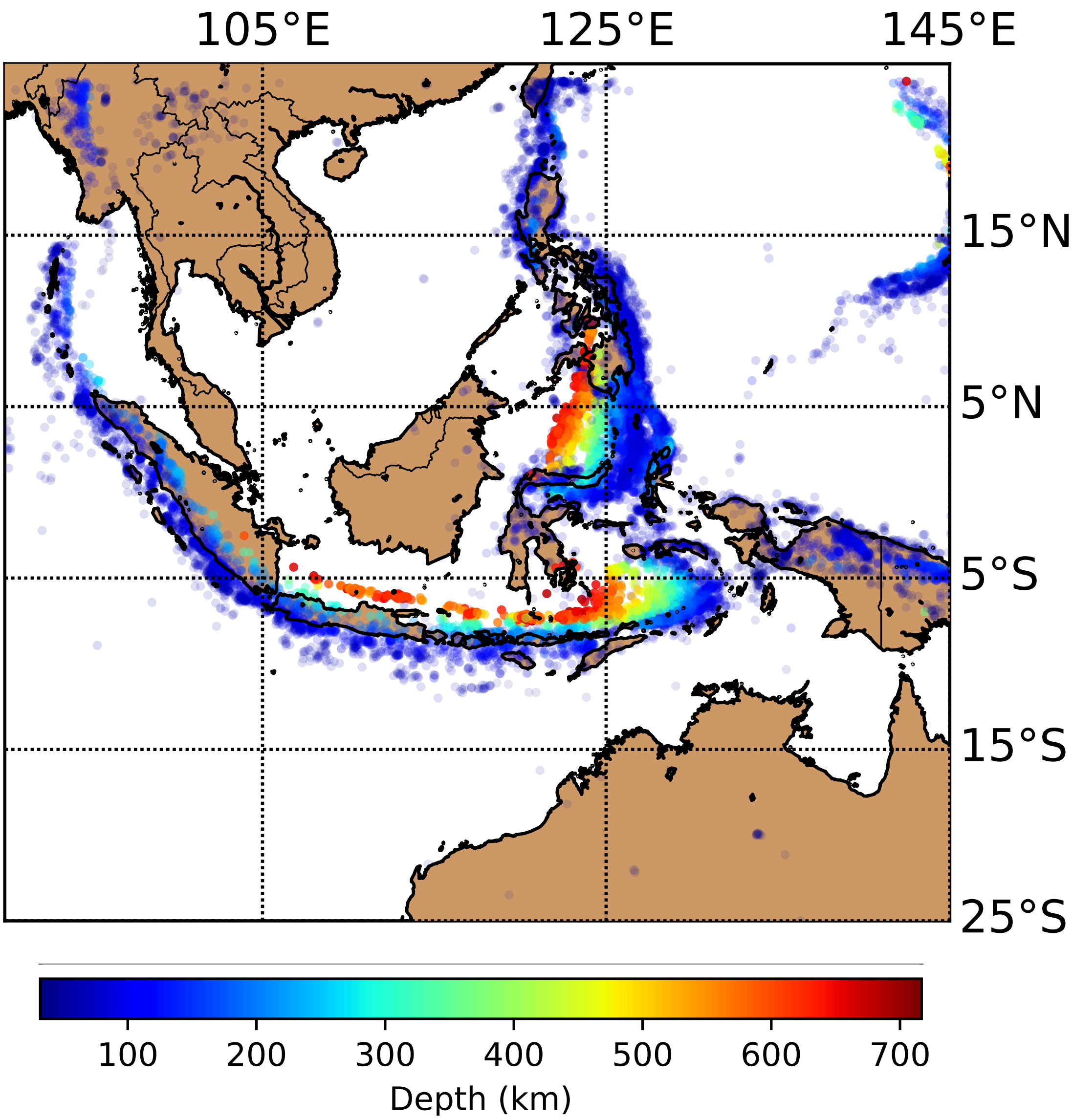

Figure 2: Regional seismicity distribution in SE Asia used for the construction of the tomographic models. For visualisation purposes greater depths are represented with greater opacity.

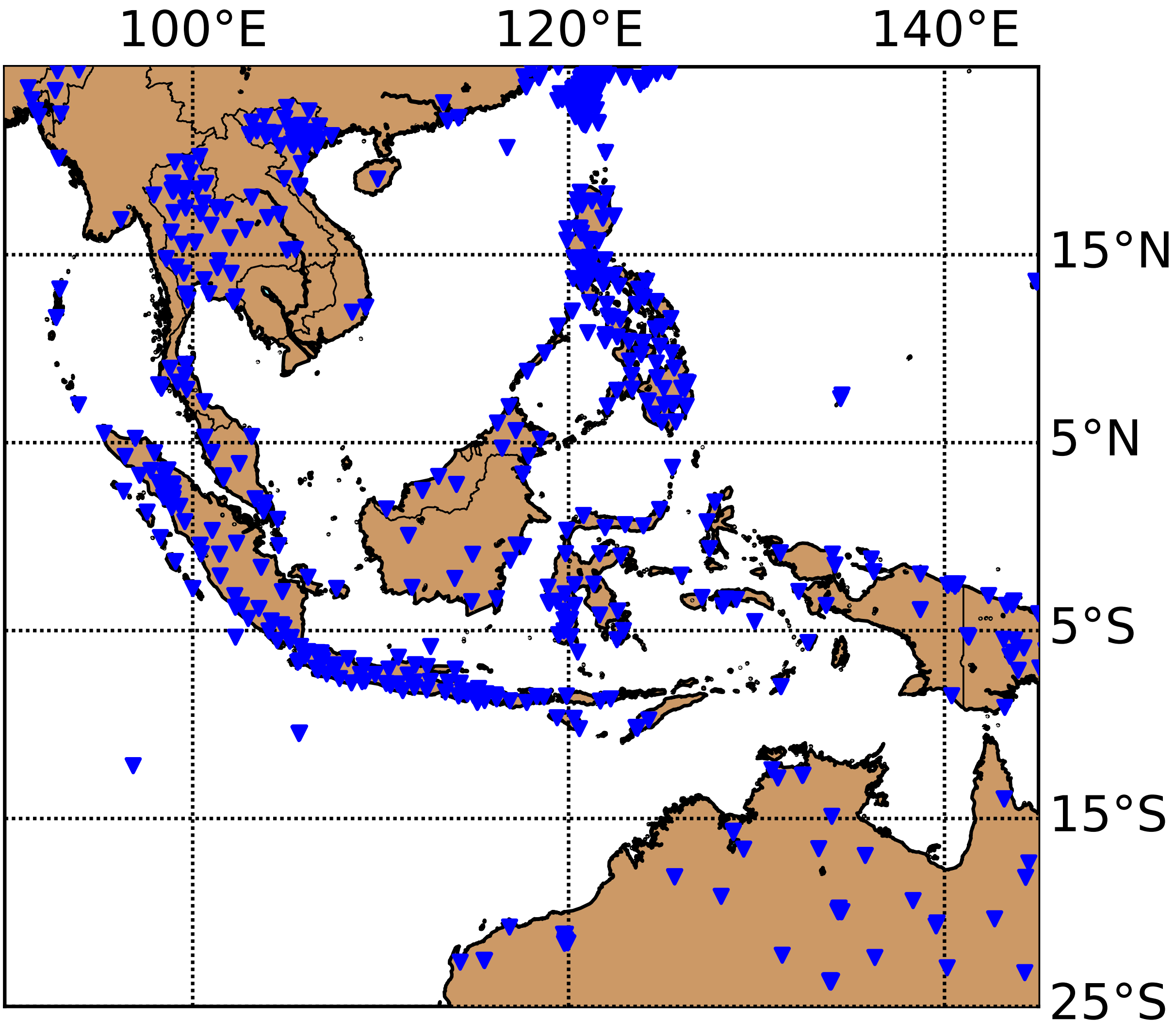

Figure 3: Map of station locations in SE Asia as used by the ISC-EHB dataset.

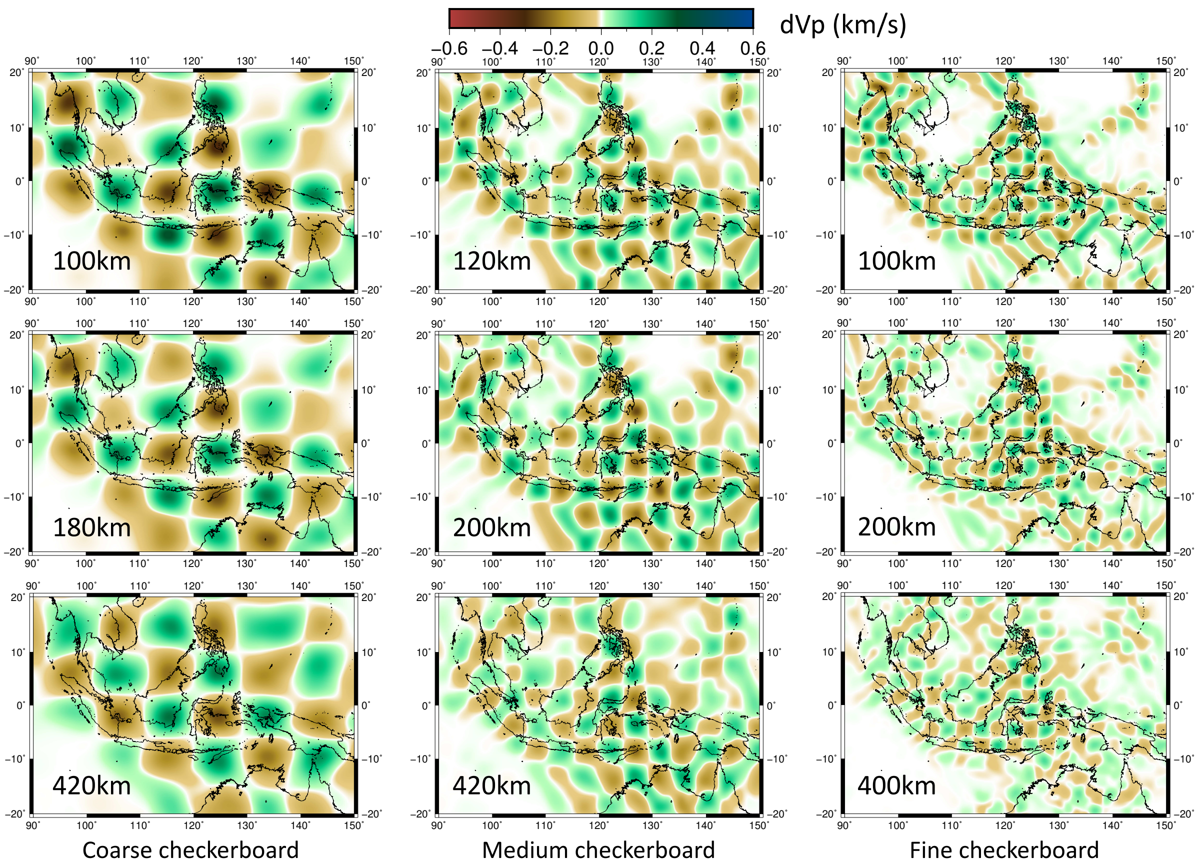

Figure 4: Results from P-wave checkerboard tests with alternating high and low velocity patterns of 0.4 km/s maximum perturbation with the P_B model source-receiver pairs.

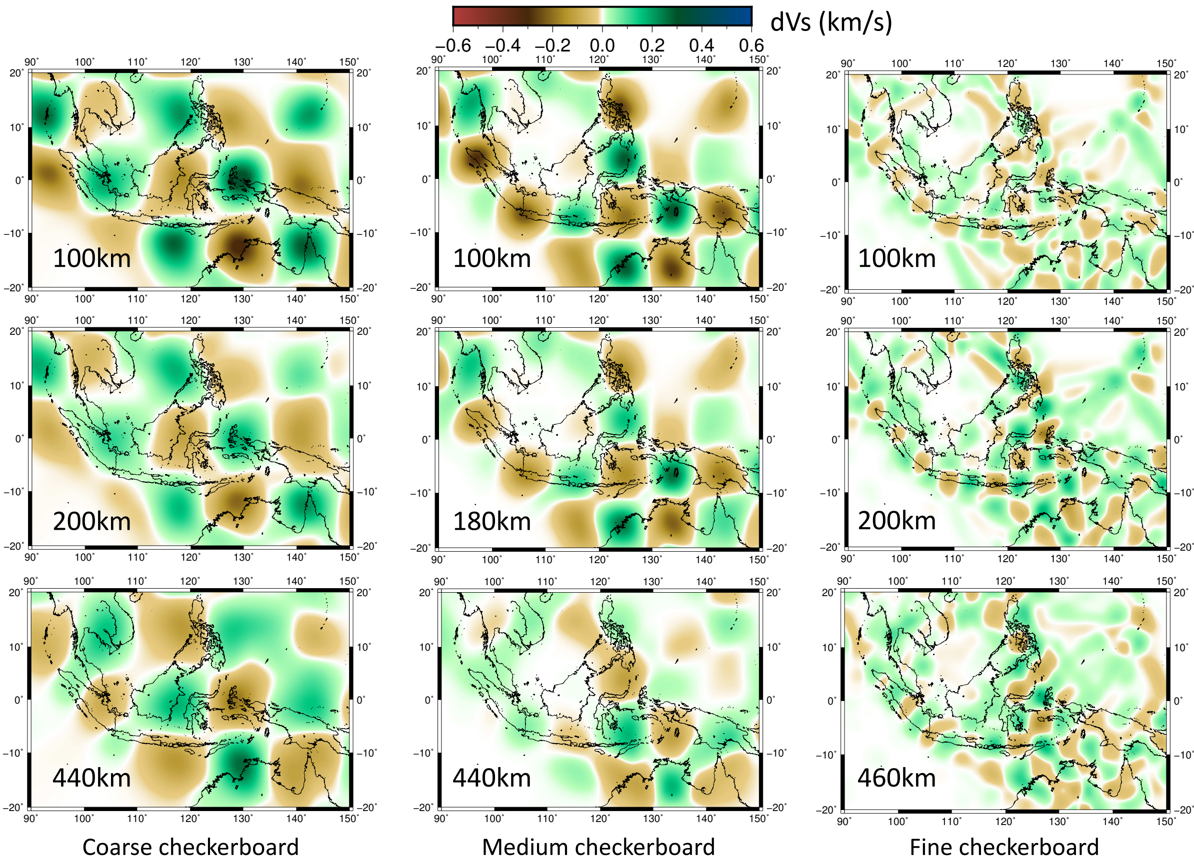

Figure 5: Results from S-wave checkerboard tests with alternating high and low velocity patterns of 0.4 km/s maximum perturbation with the S_A model source-receiver pairs.

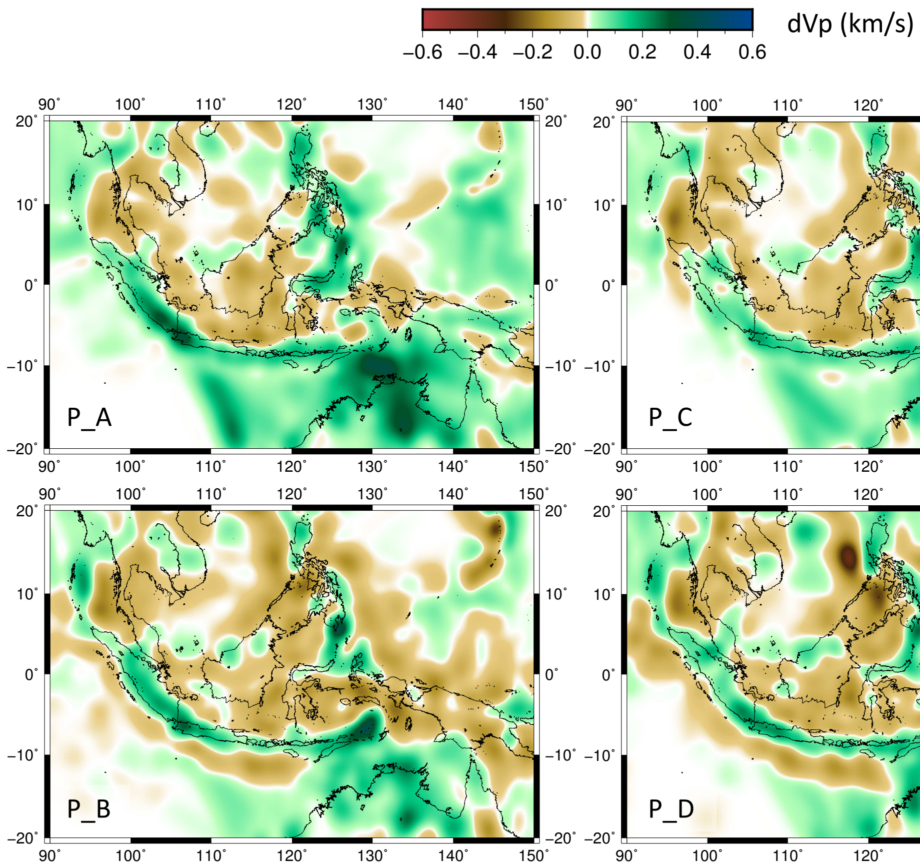

Figure 6: Comparison of the four (P_A, P_B, P_C, P_D) P-wave tomographic models using ISC-EHB-R, ISC-Reviewed-R, NLL-ISC-EHB and NLL-ISC-Reviewed datasets respectively at 200 km depth. The different input parameters used by the models are described in Table 1.

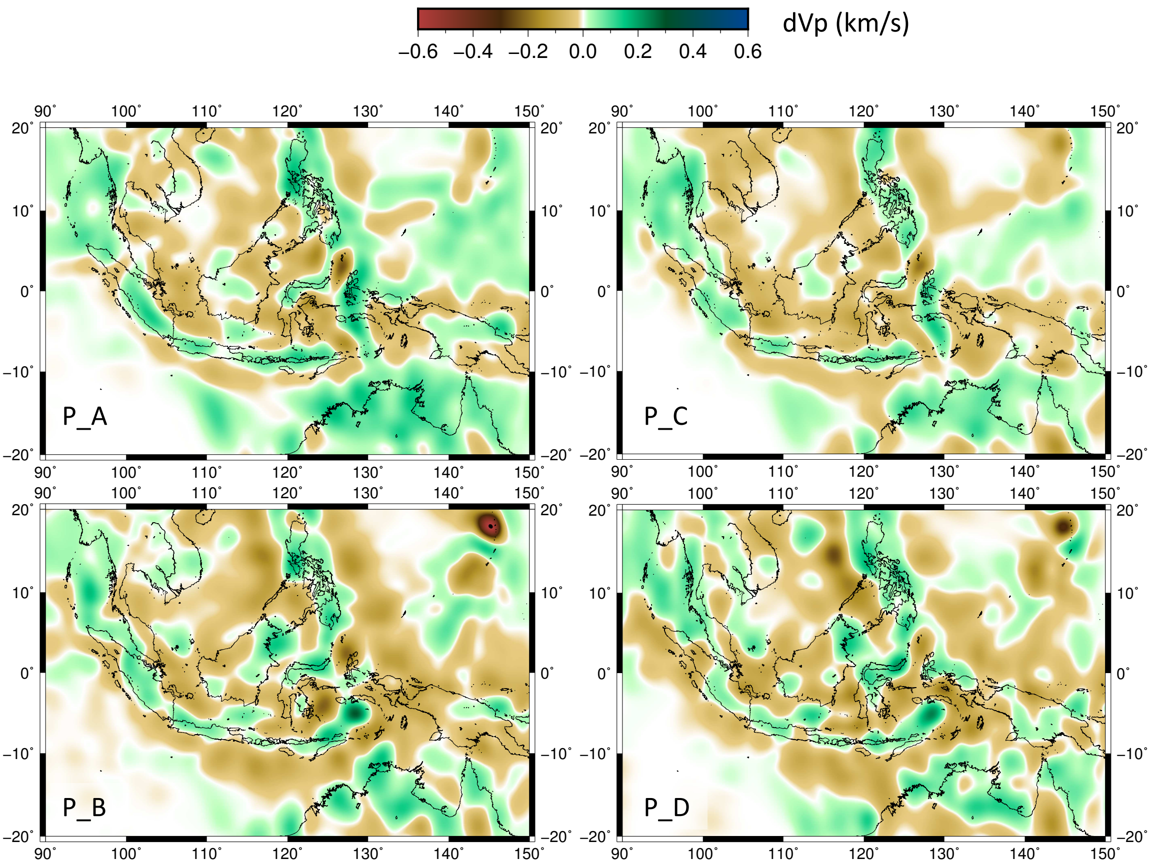

Figure 7: Same as Figure 6 but this time the model is displayed at 300 km depth. The different input parameters used by the models are described in Table 1.

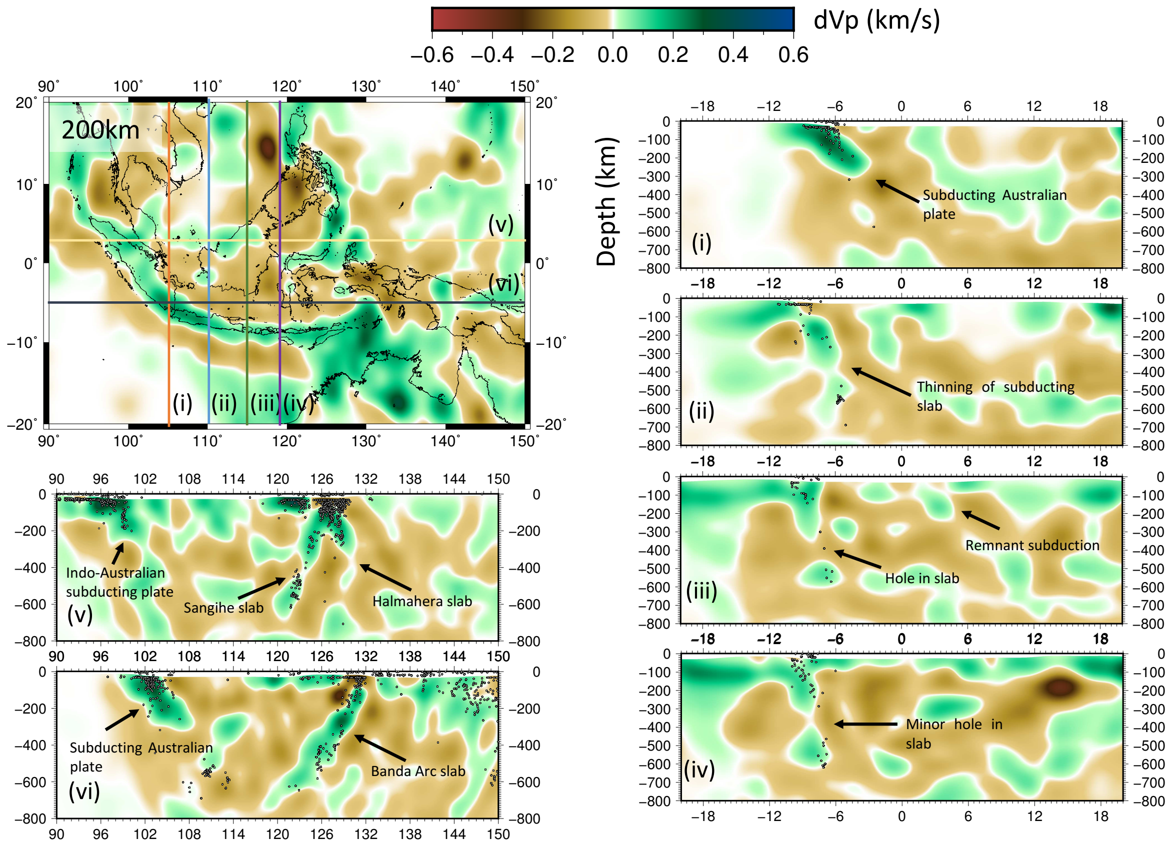

Figure 8: Cross-sections through the P-wave model using the NLL-ISC-Reviewed (P_D) dataset. Features ~~with~~ of interest are outlined with ~~a purple dashed line~~ labelled arrows in the cross-sections through the model. Various slices show different features in the region: (i) subduction along Sumatra, (ii) slab ~~in~~ beneath Java region, (iii) major hole in the slab below east Java, (iv) minor hole in the slab east of the major hole, (v) Sangihe and Halmahera arc-arc collision and the start of the subducting slab in northwestern Sumatra, (vi) curved subduction near Banda arc and the subducting slab ~~in~~ below Sumatra near the ~~tear (see~~ break as discussed in section ~~1)~~4.3.2.

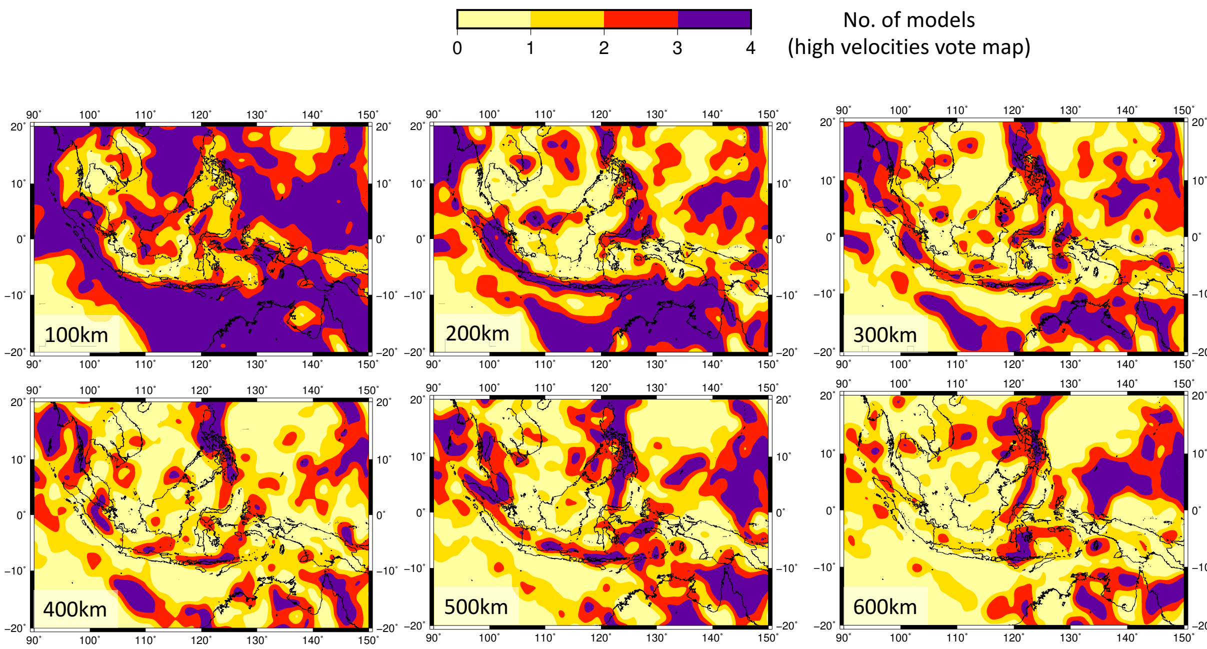

Figure 9: Votemap for all four models produced by the different P-wave datasets (P_A, P_B, P_C, P_D). High velocities ($dv/v > 0$) were assigned the value 1 for each model. Thus, in places where all the models exhibit a positive perturbation, the votemap has a value of 4, and where all the models exhibit a negative perturbation, the votemap has a value of zero.

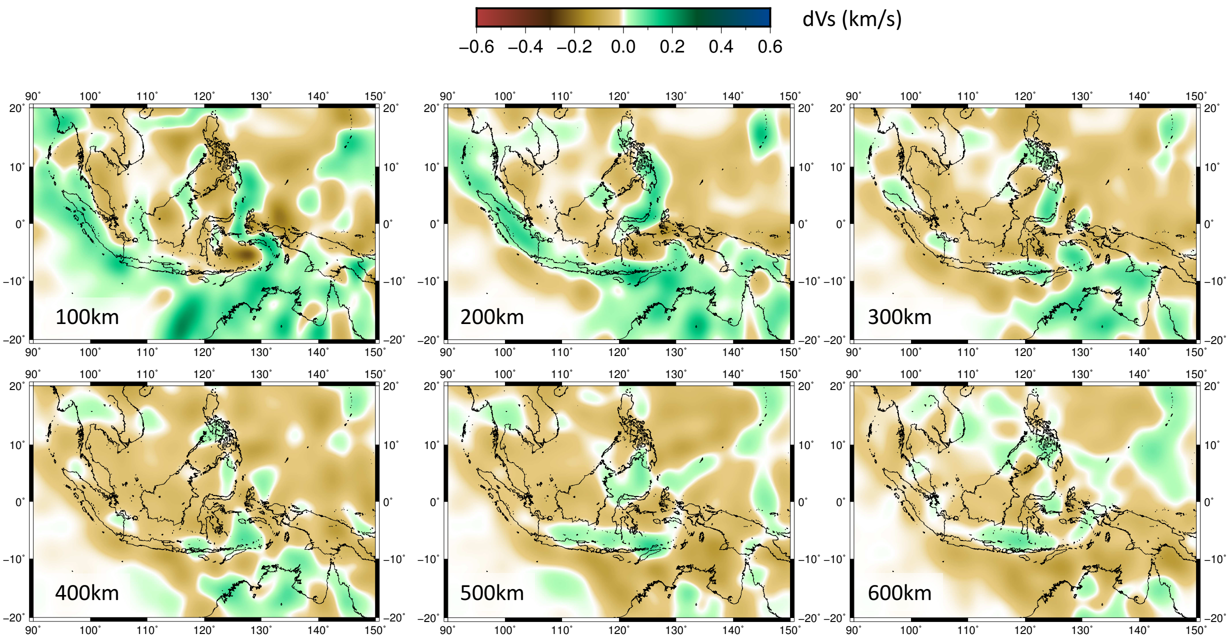

Figure 10: S-wave tomographic model using ISC-EHB (S_A) dataset from 100-600 km depth.

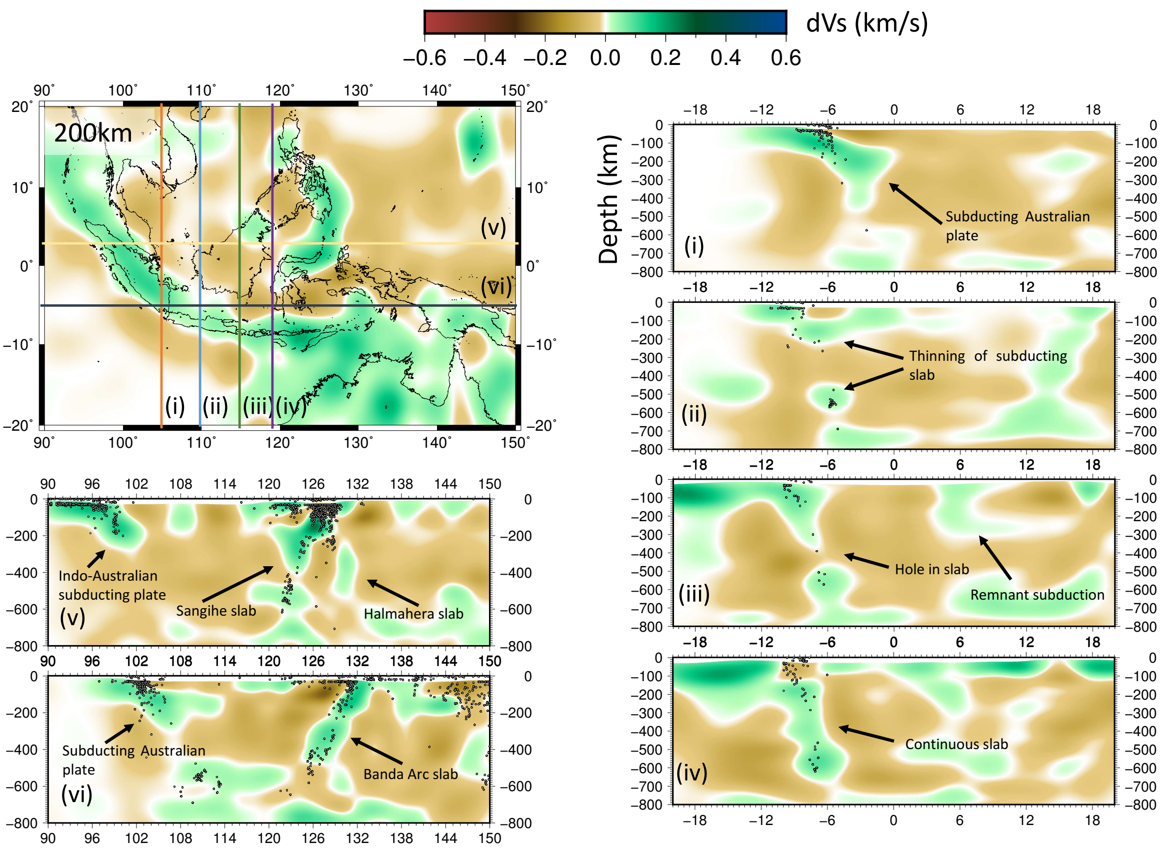

Figure 11: Cross-sections through the S-wave model based on the ISC-EHB (S_A) dataset. The S-wave dataset has a much lower number of arrivals than P, leading to lower resolution. Features of interest are ~~outlined~~ marked with an arrow and labelled in the cross-sections through the model: (i) subduction along Sumatra, (ii) slab ~~at~~ beneath Java region, (iii) major hole in the slab near 400 km depth, (iv) slab east of Java with no evidence of small hole, (v) Sangihe and Halmahera arc-arc collision and the start of the subducting slab ~~at the~~ in northwestern ~~part~~ of Sumatra, (vi) curved subduction near Banda arc and subduction zone in Sumatra near the ~~tear~~ slab break as discussed in section ~~1~~4.3.2.